RSC Advances

PAPER

View Article Online
View Journal | View Issue

Check for updates

Cite this: *RSC Adv.*, 2023, **13**, 19046

Large-scale sonochemical fabrication of a Co_3O_4–$CoFe_2O_4$@MWCNT bifunctional electrocatalyst for enhanced OER/HER performances†

Muhammad Afaq,[a] Muhammad Shahid,[b] Iqbal Ahmad,*[c] Sheraz Yousaf,[a]
Amira Alazmi,[d] M. H. H. Mahmoud,[e] Islam H. El Azab[f]
and Muhammad Farooq Warsi*[a]

Received 10th May 2023
Accepted 10th June 2023

DOI: 10.1039/d3ra03117a

rsc.li/rsc-advances

Herein, we have prepared a mixed-phase Co_3O_4–$CoFe_2O_4$@MWCNT nanocomposite through a cheap, large-scale, and facile ultrasonication route followed by annealing. The structural, morphological, and functional group analyses of the synthesized catalysts were performed by employing various characterization approaches such as X-ray diffraction (XRD), Fourier transform infrared spectroscopy (FTIR), and scanning electron microscopy (SEM). The resultant samples were tested for bifunctional electrocatalytic activity through various electrochemical techniques: cyclic voltammetry (CV), linear sweep voltammetry (LSV), and electrochemical impedance spectroscopy (EIS). The prepared Co_3O_4–$CoFe_2O_4$@MWCNT nanocomposite achieved a very high current density of 100 mA cm^{-2} at a lower (290 mV and 342 mV) overpotential (*vs.* RHE) and a smaller (166 mV dec^{-1} and 138 mV dec^{-1}) Tafel slope in the oxygen evolution reaction (OER) and hydrogen evolution reaction (HER), respectively, compared to Co_3O_4–$CoFe_2O_4$. The excellent electrochemical activity of the as-prepared electrocatalyst was attributed to the uniform incorporation of Co_3O_4–$CoFe_2O_4$ over MWCNTs which provides high redox active sites, a greater surface area, better conductivity, and faster charge mobility. Furthermore, the enhanced electrochemical active surface, low charge-transfer resistance (R_{ct}), and higher exchange current density (J_0) of the Co_3O_4–$CoFe_2O_4$@MWCNT ternary composite are attributed to its superior behavior as a bifunctional electrocatalyst. Conclusively, this study demonstrates a novel and large-scale synthesis approach for bifunctional electrocatalysts with a high aspect ratio and abundance of active sites for high-potential energy applications.

1. Introduction

The world is trying its best to address both environmental issues and the energy crisis.[1–8] Among the concerns, electrocatalytic water-splitting has received a lot of attention because of its low power threshold, greater efficiency, and low cost. The oxygen evolution reaction (OER) and the hydrogen evolution reaction (HER) take place at the anode and cathode of the electrochemical cell, respectively, to complete the electrochemical water-splitting process.[9–11] Since the OER has slow rate kinetics and requires a high energy barrier to generate the reaction, it needs a very large overpotential and is inefficient.[10] The HER process has been observed to have a faster rate of kinetics and require very low overpotential.[12] Materials based on noble metals, such as ruthenium and iridium oxides for the oxygen evolution reaction and platinum for the hydrogen evolution reaction, exhibit impressive water-splitting efficiency, but they are not practical for widespread use due to their scarcity, high cost, and short longevity.[13–15] Therefore, in the last few decades, there has been a lot of focus on developing and manufacturing electrocatalysts that are highly efficient, extremely accessible, and very cheap for high-efficiency water splitting. In particular, oxides, chalcogenides, phosphides, and metal–organic frameworks (MOFs) based on transition metals have gained popularity due to their superior performances and extended durability.[16–19] Since the above-discussed state-of-the-art electrocatalysts only show performance in one of these areas, it is both difficult and exciting to design a dual functional

---

[a] *Institute of Chemistry, Baghdad-ul-Jadeed Campus, The Islamia University of Bahawalpur, Bahawalpur, 63100, Pakistan. E-mail: farooq.warsi@iub.edu.pk*
[b] *Department of Chemistry, College of Science, University of Hafr Al Batin, P.O. Box 1803, Hafr Al Batin, Saudi Arabia*
[c] *Department of Chemistry, Allama Iqbal Open University, Islamabad, 44000, Pakistan. E-mail: Iqbal.ahmad@aiou.edu.pk*
[d] *Department of Science and Technology, University Colleges at Nairiyah, University of Hafr Al Batin, Nairiyah 31981, Saudi Arabia*
[e] *Department of Chemistry, College of Science, Taif University, Taif 21944, Saudi Arabia*
[f] *Department of Food Science and Nutrition, College of Science, Taif University, P.O. Box 11099, Taif 21944, Saudi Arabia*

† Electronic supplementary information (ESI) available. See DOI: https://doi.org/10.1039/d3ra03117a

catalyst that can concurrently catalyze both hydrogen evolution and oxygen evolution reaction.[20]

Iron (Fe), cobalt (Co), and nickel (Ni)-based electrocatalysts have been the subject of extensive research in electrocatalysis processes because of their affordability, widespread accessibility, ease of fabrication, and high efficiency during electrocatalytic processes.[21,22] Particularly, bi- and trimetallic derivatives were found to be significantly superior to their monometallic analogs, possibly owing to improved permeability, strong interaction, and surface electrical state. Also, many cobalt and iron-based oxides have high water oxidation potentials, but surprisingly, only a small percentage of these materials are also bifunctional.[23] Transition metal oxides (TMOs) have poor conductance and structural stability, which prevents them from performing their dual roles. Despite this, several research teams have found solutions to these problems by constructing TMO nanostructures with a massive proportion of exposed specific surface area, a high concentration of oxygen vacancies, and the exposure of particular crystal faces. This has allowed them to add strong HER activity to the impressive OER activity they already had.[21,24,25]

When looking at electrocatalysts for water splitting, cobalt ferrite ($CoFe_2O_4$) stands out as a possible option due to its low price and high catalytic activity.[26] Catalysts based on cobalt are particularly attractive choices because the addition of other metals to their lattice structure has the potential to greatly increase their efficiency.[26] Spinels based on cobalt are highly stable and can transport a charge, making them a promising substrate for low-cost, readily available electrocatalysts. In particular, $CoFe_2O_4$ with a partially inverted spinel structure has been studied for its potential as an OER catalyst, and its function can be modified *via* hybridization, morphology engineering, and size modification.[27–29]

Carbon-based water-splitting catalysts have gained a lot of popularity recently due to their cost effectiveness, easy accessibility, and little influence on the environment. One prominent factor is a multi-walled carbon nanotube (MWCNT)-based composite for bifunctional electrocatalytic activity as it enhances the material conductivity, increases mass and charge transfer, and provides an abundance of active sites for superior electrocatalytic activity.[30] Owing to their superior aspect ratio, electrical conductivity, superior mechanical strength, and persistence, MWCNTs are an appealing carbonaceous material as a solid support for heterogeneous catalysts.[31] Several methods have been suggested for fabricating mixed-phase binary and ternary nanocomposite (solid-state, sol–gel, hydrothermal, co-precipitation, *etc.*).[32–35] The benefits of ultrasonic irradiation synthesis include large-scale synthesis, reduced reaction times, smaller product sizes, more precise control over synthesis conditions, less manufacturing costs, higher grade standards, less environmental effect, and so on.[36] Acoustic cavitation, the process by which bubbles form, expand, and then combust as a result of ultrasound irradiation, is responsible for most of the chemical effects of this type of irradiation. The high energy density created by the bubble contents being heated by the liquid kinetic energy during the collapse can supply the necessary energy for chemical reactions. So, it is possible to consider it as an alternative to the more typical ways of synthesis.[37,38]

In this work, we have presented a simplified ultrasonication route for the fabrication of dual-phased Co_3O_4–$CoFe_2O_4$ and multi-walled carbon nanotubes loaded Co_3O_4–$CoFe_2O_4$ electrocatalyst. Multifunctional properties toward HER/OER reactions have been demonstrated by the optimized Co_3O_4–$CoFe_2O_4$@MWCNT composite by requiring very low overpotential to reach high current density. The synergistic effect between dual-phased Co_3O_4–$CoFe_2O_4$ and MWCNTs, beyond their primacy in structural and physical features, effectively boosts the electrocatalytic activity.

2. Experimental section

2.1. Required reagents

All chemical compounds; cobalt nitrate hexahydrate ($Co(NO_3)_2\cdot 6H_2O$), polyethylene glycol (PEG), sodium carboxymethyl cellulose (CMC), ethanol (C_2H_5OH), multi-walled carbon nanotubes (MWCNTs), deionized water, and iron nitrate nonahydrate ($Fe(NO_3)_3\cdot 9H_2O$) were procured from Sigma-Aldrich. There was only analytical-grade chemistry available and of the highest purity.

2.2. Preparation of Co_3O_4–$CoFe_2O_4$ binary nanocomposite

The dual-phased Co_3O_4–$CoFe_2O_4$ nanoparticles were synthesized *via* a simple sonochemical activation technique. Ultrasonication was performed for 2 hours on a crucible containing iron nitrate nonahydrate (5.56 g), cobalt nitrate (2 g), and polyethylene glycol (20 g/24 mL of DI water). The crucible was then annealed for 2 hours at 700 °C. The resultant Co_3O_4–$CoFe_2O_4$ nanoparticles were obtained after annealing.

2.3. Preparation of Co_3O_4–$CoFe_2O_4$@MWCNT ternary nanocomposite

The ternary nanocomposite of multi-walled carbon nanotubes and mixed-phase Co_3O_4–$CoFe_2O_4$ was made using an easy-to-implement ultrasonication method. Firstly, 20 mg of MWCNTs were well-dispersed into deionized water by employing a sonication of one an hour. After that, 180 mg of the as-prepared Co_3O_4–$CoFe_2O_4$ sample was added slowly into the above MWCNTs suspension solution. Then the co-dissolved mixture was again treated with ultra-sonication for 120 minutes to obtain a homogenous mixture and excellent dispersion among the materials. The obtained sample was then dried at 80 °C and used for electrochemical performances.

2.4. Preparation of electrodes

The measured small pieces of carbon fiber cloth (CFC) were taken and then washed with ethanol and acetone, followed by distilled water. Afterward, electrocatalyst ink was made by dispersing 15 mg of as-synthesized materials in a 100 μL mixture of sodium carboxymethyl cellulose (CMC) binder and distilled water. The mixture was well-sonicated for 2 h. Electrodes for electrochemical assessments have been prepared by loading a CFC selective area (1 cm^2) with 10 μL of electrocatalyst ink using the drop-casting method.

2.5. Characterization

The structural analysis and crystalline nature of as-fabricated materials were performed by using Lab XRD-6100 powder X-ray diffraction (XRD) using Cu-Kα as a source of radiation having $\lambda = 1.54$ Å and equipped with a position-sensitive detector. The morphological analysis of prepared samples was carried out using a scanning electron microscope (FEI Inspect S50; SEM). Fourier transform spectroscopy (FTIR) was deployed to examine the vibrational modes of prepared materials using a Shimadzu IR Affinity-1S spectrometer with KBr pellets approach.

2.6. Electrochemical water splitting assessment

The as-prepared electrocatalysts were tested in a conventional three-electrode setup in an alkaline solution of 1.0 M potassium hydroxide by using Gamry (INTERFACE 5000 E Potentiostat) electrochemical workstation to evaluate their electrocatalytic activity for bifunctional electrocatalytic activity. A mercury/mercury oxide (Hg/HgO) reference electrode, an electrocatalyst-modified carbon fiber cloth (CFC) working electrode, and a platinum (Pt) foil as a counter electrode completed the three-electrode system. First 200 cycles of cyclic voltammetry (CV) test were performed at 100 mV s^{-1} sweep rate to activate the material then these modified CFC electrodes undergo LSV tests to gain some insight into the overpotentials at varying current densities. The LSV for OER activity of as-prepared material was observed at varying potential ranges of 0.9 to 1.7 V (*vs.* RHE) at a scan rate of 5 mV s^{-1}. To observe the HER performance of samples, a potential of range 0 to −0.65 V (*vs.* RHE) was applied at 5 mV s^{-1}. The obtained potential values by using standard Hg/HgO electrodes were converted into reversible hydrogen electrode potentials (E_{RHE}).[39] The estimated pH for the alkaline solution used was 13.5. Furthermore, we have derived the Tafel slopes ($\log j$ *vs.* OP) of nano-catalysts from their correlating LSV curves to better comprehend the reaction's viability. The cyclic voltammetry investigations were performed at five diverse scan rates in a non-faradic capacitive current range to estimate the double layer-capacitance (C_{dl}) values of as-fabricated Co_3O_4–$CoFe_2O_4$ and Co_3O_4–$CoFe_2O_4$@MWCNT catalysts. By further exploitation of the C_{dl} value, we have calculated the average C_{dl} values and electrochemically active surface area of materials by employing the formula; Average $C_{\mathrm{dl}}/C_{\mathrm{s}}$, where C_{s} is the specific capacitance of semiconducting materials (0.040 cm^{-2}).[40,41] Moreover, the EIS spectroscopic technique was used to assess the mass and charge transfer capabilities of CFC-modified electrocatalyst electrodes between solid and liquid interface resistance over a frequency range of 100 000 to 0.1 Hz. A Co_3O_4–$CoFe_2O_4$@MWCNT-loaded CFC substrate was then subjected to extensive chronopotentiometry testing (720 minutes) to determine the long-term performance and stability of the as-fabricated bifunctional electrocatalyst.

3. Results and discussion

3.1. Structural analysis

The synthesis of as-prepared samples was confirmed by using the powder-X-ray diffraction technique. The crystal structure, phase, and crystallite size analyses were also investigated by interpretation of XRD data from the obtained nanostructures. The XRD diffraction patterns of as-obtained Co_3O_4–$CoFe_2O_4$ and Co_3O_4–$CoFe_2O_4$@MWCNTs are presented in Fig. 1. The diffraction patterns present at 2θ values = 35.5°, 43.2°, 53.8°, and 56.5° correspond to (311), (400), (422), and (511) crystal planes of characteristic cobalt ferrite (JCPDS card no. 01-077-0426; space group $Fd\bar{3}m$) with cubic crystal phase.[42] The cobalt oxide (Co_3O_4) diffraction patterns were observed at 2θ values of 23.4°, 31.6°, and 45.5° can be assigned to (200), (220), and (400) crystal planes,[43] well-matched with standard JCPDS card no. 01-071-0816. This confirms the presence of cubic phase Co_3O_4 nanoparticles in the produced sample and the formation of a mixed-phase $CoFe_2O_4$–Co_3O_4 nanostructure. The combination of two phases leads to enhanced electrocatalytic activity due to the combined synergistic effect of these nanostructures. The Co_3O_4–$CoFe_2O_4$@MWCNTs XRD plot shows a prominent hump at $2\theta = 25.4°$, which confirms the existence of MWCNTs[44] in the Co_3O_4–$CoFe_2O_4$ sample. The crystallite size (D) of as-synthesized samples was estimated by using the Debye–Scherrer formula.[45]

$$D = \frac{0.9\lambda}{\beta \cos \theta} \quad (1)$$

where β refers to full-width at half maximum (FWHM), λ is the used X-rays wavelength and θ is abbreviated as corresponding diffraction angles. Co_3O_4 and $CoFe_2O_4$ nanoparticles have an estimated crystallite size of 36.18 nm and 30.8 nm, respectively. In a Co_3O_4–$CoFe_2O_4$ binary composite, the presence of Co_3O_4 particles inhibited the growth of $CoFe_2O_4$ nanoparticles by impeding the propagation of particles with different alignment and dimensions and by blocking the movement of Co and Fe ions during the growth of $CoFe_2O_4$.

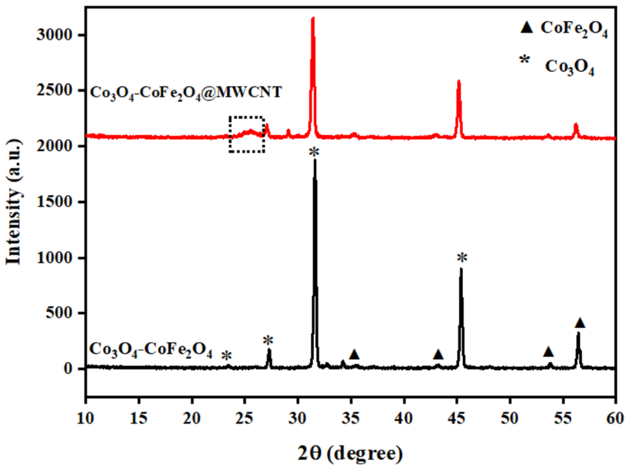

Fig. 1 XRD profiles of prepared samples: Co_3O_4–$CoFe_2O_4$ binary and Co_3O_4–$CoFe_2O_4$@MWCNT ternary nanocomposite.

Table 1 XRD lattice parameters of mixed-phase Co_3O_4–$CoFe_2O_4$ particles

S. no.	Sample	Crystal phase	Lattice constant, *a* (Å)	Lattice volume, *V* (Å^3)	Crystallite size, *D* (nm)	Specific surface area (m^2 g^{-1})
1	Co_3O_4	Cubic	8.06	523.6	36.18	610.17
2	$CoFe_2O_4$	Cubic	8.3	571.78	30.8	687.16

After analyzing the XRD data, we used the following formula to determine the specific surface area (SSA) of the Co_3O_4–$CoFe_2O_4$ sample in its as-fabricated state.[46]

$$\text{Specific surface area} = \frac{A_{sp}}{V_{particle} \times \text{density}} \quad (2)$$

whereas, A_{sp} refers to the surface area of the particle and $V_{particle}$ shows the volume of the particle. The specific surface area of the mixed-phase composition was calculated and presented in Table 1. Results exhibit that in dual-phase composition $CoFe_2O_4$ provides a higher specific surface area as compared to Co_3O_4 particles. The increased specific area of $CoFe_2O_4$ may be attributable to the fact that it has a lesser crystallite size than Co_3O_4. An increase in surface area per unit mass may result from a smaller crystallite size because of the presence of additional grain boundaries and defects. This is because as crystallite size reduces, the surface area of each crystalline domain increases.

3.2. FTIR study

Fourier transform infrared spectroscopic (FTIR) examination was executed for the determination of the bonding nature and identification of functional groups present in as-prepared materials. FTIR analysis was performed in the range of 4000–400 cm^{-1}. The FTIR spectra of Co_3O_4–$CoFe_2O_4$ and Co_3O_4–$CoFe_2O_4$@MWCNT nanomaterials are presented in Fig. 2. The peaks located around 690 cm^{-1} in FTIR spectrum are corresponded to stretching vibration mode of metal–oxygen absorption band.[47,48] The band around 1114 cm^{-1} is assigned to the cobalt–iron alloy system.[49] These absorption bands confirm the preparation of dual-phase Co_3O_4–$CoFe_2O_4$ nanomaterial. The peaks around 873 cm^{-1} and 1427 cm^{-1} were referred to as vibrational modes of the C–O group which may be present due to the adsorption of atmospheric CO_2.[48,50] The broad bands located at 2926 cm^{-1} and 3665 cm^{-1} was assigned to the stretching vibrations of the O–H bond.[49,50] The peak shifting was observed in the FTIR spectrum of Co_3O_4–$CoFe_2O_4$@MWCNT nanostructures, which confirms the synthesis of a ternary nanocomposite.

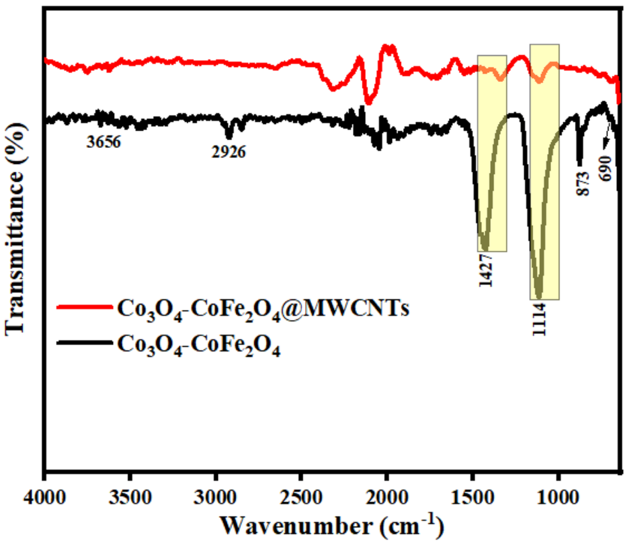

Fig. 2 Illustrates the FTIR spectra of fabricated materials in the 4000–400 cm^{-1} range.

3.3. Morphology studies

SEM analysis was performed to observe the morphologies of as-prepared Co_3O_4–$CoFe_2O_4$ and Co_3O_4–$CoFe_2O_4$@MWCNT electrocatalysts. Fig. 3(a) and (b) display the SEM profiles of Co_3O_4–$CoFe_2O_4$ and Co_3O_4–$CoFe_2O_4$@MWCNT, respectively, after fabrication. The SEM patterns in Fig. 3(a) show that the as-fabricated Co_3O_4–$CoFe_2O_4$ nanostructures have a rock-like amorphous morphology with defined lateral boundaries. The rock-like morphology is composed of basic disc-shaped units that combine together, giving rise to the observed structure. The average diameter of the rock-like amorphous structures was calculated and is approximately 3.5 μm. Furthermore, we have also calculated the average diameter of the voids within the composite material, which was found to be approximately 0.87 μm. Possibly as a result of the ultra-sonochemical fabrication of Co_3O_4–$CoFe_2O_4$@MWCNT, the nano-rocks of Co_3O_4–$CoFe_2O_4$ are evenly dispersed over the MWCNT in Fig. 3(b). With the help of ultra-sonication, nano-rock structures on nanotubes can interact and dissipate in a more homogeneous approach. And as seen in Fig. 3(a) and (b), there are several voids that may promote electrocatalytic activity.

3.4. Preliminary electrochemical tests

The electrochemical stability of as-fabricated electrocatalysts was tested before their bifunctional electrocatalytic performance in terms of electrochemical active surface area, stability, and availability of active sites using the electrochemical method. The cyclic voltammetry tests were performed to analyze the redox peaks in as-produced electrocatalyst-loaded CFC substrate and unmodified CFC.[51] The obtained cyclic voltammogram results of as-prepared Co_3O_4–$CoFe_2O_4$ and Co_3O_4–$CoFe_2O_4$@MWCNT nanostructures demonstrate clear broad redox peaks, while no redox peaks were observed in the case of bare CFC. Furthermore, 200 consecutive cycles of CV (Fig. S1†) at a sweep rate of 100 mV s^{-1} on the fabricated materials were

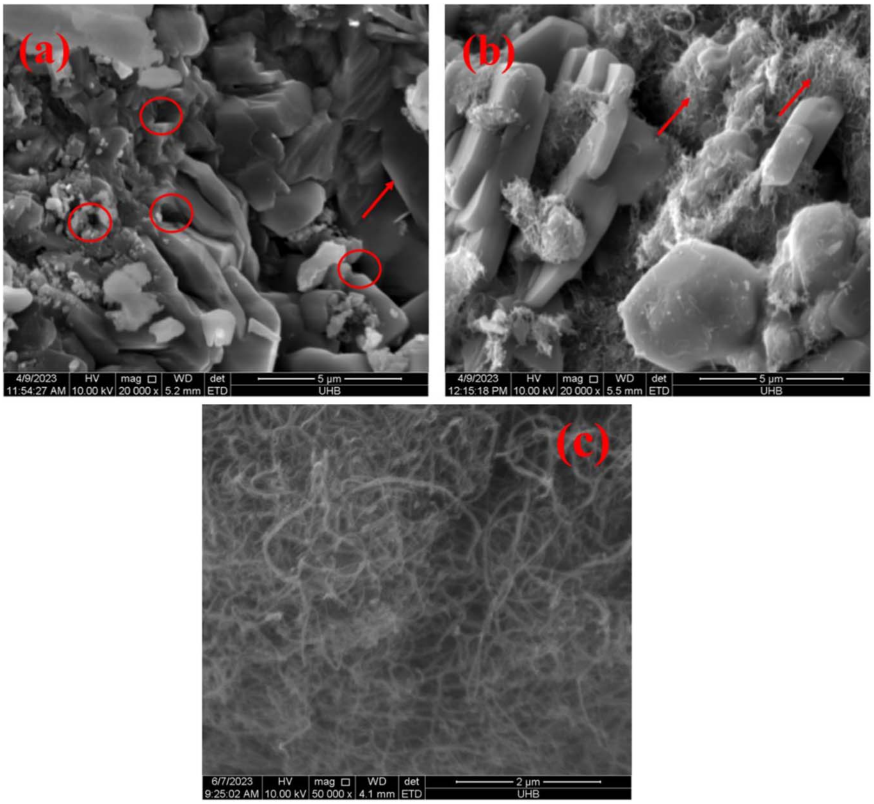

Fig. 3 SEM profiles of as-prepared samples: (a) Co_3O_4–$CoFe_2O_4$, (b) Co_3O_4–$CoFe_2O_4$@MWCNT nanostructures and (c) pure MWCNTs.

carried out to evaluate the activity, stability, and aging of the fabricated materials. The area under the CV loop was directly related to charge (q^*). The CV plots suggest no change in current density with a very small change in their shape. The charge (q^*) associated with these successive cycles was determined and found to be constant with the increase in the number of cycles as shown in Fig. 4. The constant charge (q^*) suggests that there was no potential loss of active sites, and all-fabricated samples are stable, effective, and have successive electrochemical activity for overall water splitting. The charge fraction (q^*/q^*_{initial}) was estimated for all materials. The obtained fraction results were uniform for all prepared materials during successive 200 CV cycles. The charge fraction (q^*/q^*_{initial}) plots were presented in Fig. 3. The electrocatalytic sites were considered to be in direct relation with charge,[52] therefore, the charge fraction analysis was carried out to check the overall water splitting performance of prepared electrocatalysts. Lastly, the above preliminary results demonstrate that materials have acquired the required stability and can be used for further electrochemical investigations.

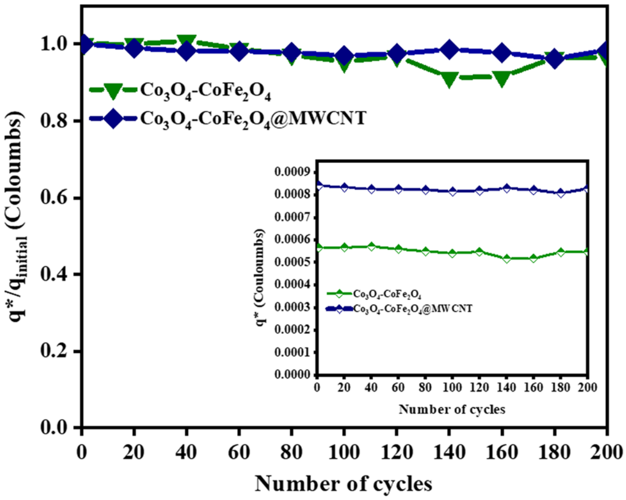

Fig. 4 Electrochemical measurements of the as-prepared sample, q^*/q^*_{initial} fraction for concurrent 200 CV cycles at 100 mV s^{-1}. The inlays in the figure demonstrate the charge (q^*) evaluation of consecutive cycles.

Moreover, to further investigate the performance of electrocatalysts, the surface concentration of atoms was calculated using cyclic voltammograms taken at a sweep rate of 20 mV s^{-1}. The area under the reduction peak of the CV plot was considered and presented in Fig. S2.† The charge enclosed by the ternary composite reduction peak at 20 mV s^{-1} was found to be greater than the bare Co_3O_4–$CoFe_2O_4$ sample. The Co^{2+}/Co^{3+} redox couple was linked by the charge enclosed in the reduction peak. And it was assumed that one cobalt atom could only chemically adsorb one oxygen atom. The Co_3O_4–$CoFe_2O_4$@MWCNT ternary composite has a higher reduction peak area than the other tested sample. The Co_3O_4–$CoFe_2O_4$@MWCNT electrocatalyst has a higher calculated surface concentration of atoms due to a greater reduction peak area as compared to Co_3O_4–$CoFe_2O_4$ and displayed in Table 2.

Table 2 Preliminary electrochemical parameters of as-prepared materials

S. no.	Parameters	Co_3O_4–$CoFe_2O_4$	Co_3O_4–$CoFe_2O_4$@MWCNT
1	Average C_{dl} (cm^{-2})	0.13	0.26
2	ECSA (cm^2)	3.25	6.56
3	The surface concentration of atoms ($\times 10^{15}$)	1.31	6.24

The electrochemical active surface area (ECSA) of electrocatalysts was also considered in terms of electrocatalytic active sites by using the CV approach. The fabricated Co_3O_4–$CoFe_2O_4$ and Co_3O_4–$CoFe_2O_4$@MWCNT materials cyclic voltammograms were recorded for the non-faradaic region at varying scan rates (mV s^{-1}) which are shown in Fig. S3.† The graphs between scan rate *vs.* current (A) were used for the estimation of ECSA of resultant samples and are presented in Fig. 5. The slope of these linear plots was considered to be C_{dl}. The average C_{dl} of fabricated materials was calculated and presented in Table 2. The higher average C_{dl} value of Co_3O_4–$CoFe_2O_4$@MWCNT shows that it provides a higher electroactive surface area for electrochemical performances. Furthermore, the ternary nanocomposite has greater available ECSA (6.56 cm^2) as compared to its counterpart (3.25 cm^2), which means it provides a highly porous shape and more exposed electroactive sites, which are responsible for excellent OER and HER performances.

3.4.1. Electrocatalytic OER and HER performances. The OER activity of RuO_2, Co_3O_4–$CoFe_2O_4$, and Co_3O_4–$CoFe_2O_4$@MWCNT samples was assessed by LSV tests at a sweeping rate of 5 mV s^{-1} with automatic *iR* compensation. For comparison, measurements of pure CFC and CFC-loaded sodium carboxymethyl cellulose (CMC) binder were also taken. The LSV curves of RuO_2, Co_3O_4–$CoFe_2O_4$, and Co_3O_4–$CoFe_2O_4$@MWCNT obtained from the OER run are displayed in Fig. 6(a). In addition, a thorough analysis of the electrocatalyst performance was conducted to pinpoint the catalyst responsible for the observed current density of 100 mA cm^{-2}. The observed overpotential for RuO_2, Co_3O_4–$CoFe_2O_4$, and Co_3O_4–$CoFe_2O_4$@MWCNT 320 mV, 333 mV, and 290 mV, respectively, at 100 mV s^{-1} current density. The lower overpotential value of Co_3O_4–$CoFe_2O_4$@MWCNT reflects improved OER performance than the rest of the samples. Extensive data about the sample's electrocatalytic behavior and mechanism was obtained by calculating their Tafel slopes using the LSV polarization curves.

Tafel slopes for RuO_2, Co_3O_4–$CoFe_2O_4$, and Co_3O_4–$CoFe_2O_4$@MWCNT samples are 123, 220, and 166 mV dec^{-1}, respectively (Fig. 6(b)). The smallest Tafel slope value of the Co_3O_4–$CoFe_2O_4$@MWCNT electrocatalyst reflects the improved electrocatalytic behavior and excellent kinetics toward OER. Tafel plots were also used to determine the OER mechanism taking place at the electrode surface.[53] The OER mechanism involves the adsorption of hydroxyl groups on Co_3O_4–$CoFe_2O_4$@MWCNT active sites. Mainly 4 steps are involved which are depicted in eqn (3)–(6) during the whole mechanism. In the very first step, hydroxyl radicals are formed from hydroxyl anions on the active sites (M*) of the electrocatalyst. In the second step, the hydroxyl radicals were converted into reactive oxygen radicals (M–O*) with the removal of electrons and water molecules. Another nucleophilic hydroxyl radical attacks on M–O* and converts it into M–OOH* with the release of electrons during the third step. In the last step, the formed M–OOH* radical then again reacts with OH^- anion to generate an oxygen molecule, metal active site, water molecule, and electron. In summary, the oxygen generation mechanism of Co_3O_4–$CoFe_2O_4$@MWCNT involves four hydroxyl anions with the release of two water molecules and electrons.[54,55]

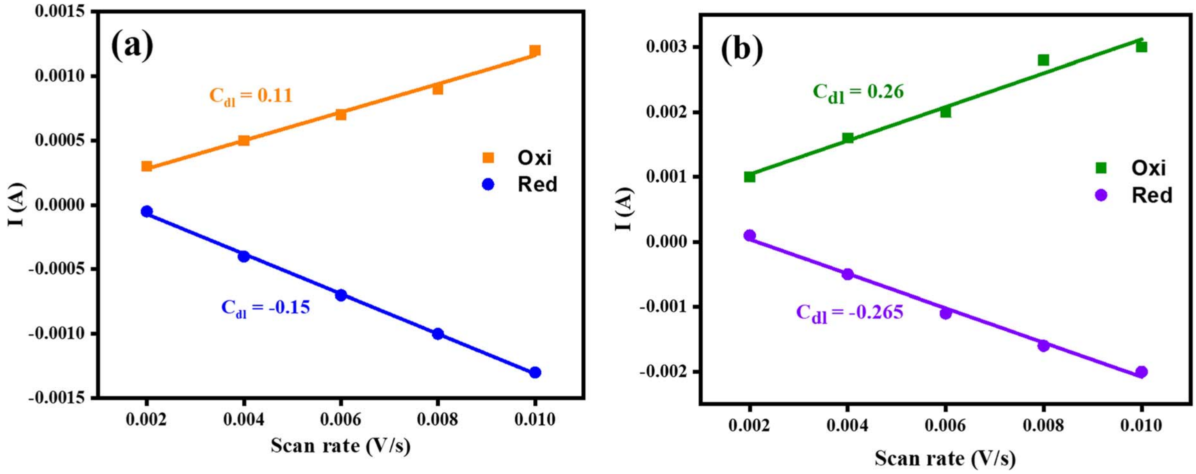

Fig. 5 Graphs of fabricated materials for the determination of ECSA; (a) mixed-phase Co_3O_4–$CoFe_2O_4$ (b) Co_3O_4–$CoFe_2O_4$@MWCNT electrocatalysts.

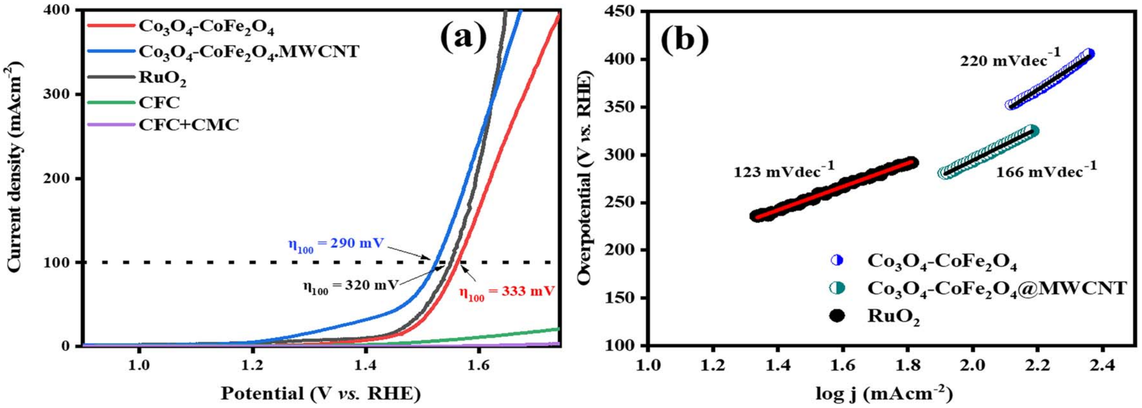

Fig. 6 (a) LSV polarization curves of CFC, CFC with the binder, RuO_2, Co_3O_4–$CoFe_2O_4$, and Co_3O_4–$CoFe_2O_4$@MWCNT electrocatalysts at scan rate 5 mV s^{-1} for catalytic oxygen evolution reactions activity and (b) respective Tafel slopes.

$$OH^- + M^* \leftrightarrow M\text{–}OH^* + e^- \tag{3}$$

$$M\text{–}OH^* + OH^- \leftrightarrow M\text{–}O^* + H_2O + e^- \tag{4}$$

$$M\text{–}O^* + OH^- \leftrightarrow M\text{–}OOH^* + e^- \tag{5}$$

$$M\text{–}OOH^* + OH^- \leftrightarrow \text{oxygen}\uparrow + M^* + H_2O + e^- \tag{6}$$

Overall mechanism:

$$4(OH)^- \rightarrow O_2\uparrow + 2H_2O + e^- \tag{7}$$

To evaluate the HER activity of samples, the HER polarization curves of Co_3O_4–$CoFe_2O_4$ and Co_3O_4–$CoFe_2O_4$@MWCNT were compared with those of a state-of-the-art Pt foil, bare CFC, and CFC deposited with the binder. The HER profiles of Pt, Co_3O_4–$CoFe_2O_4$, and Co_3O_4–$CoFe_2O_4$@MWCNT are exhibited in Fig. 7(a). It was found that pure CFC and CFC + CMC electrodes had negligible HER activity. Therefore, modified electrocatalysts performed normally during electrocatalytic reactions, regardless of the presence of CFC. The electrochemical performance of the prepared material was demonstrated by measuring the overpotential. The observed OP for Co_3O_4–$CoFe_2O_4$@MWCNT (342 mV) in hydrogen evolution experiments at current density 100 mA cm^{-2} is lower than pristine Co_3O_4–$CoFe_2O_4$ (419 mV) which demonstrates its high intrinsic HER activity. Tafel slopes were also calculated by using LSV data and shown in Fig. 7(b) which represents the stage in the electrocatalytic hydrogen generation process that establishes the rate and the likely mechanism. Tafel slope values were measured to be 69 mV dec^{-1} for Pt foil, 151 mV dec^{-1} for Co_3O_4–$CoFe_2O_4$, and 138 mV dec^{-1} for Co_3O_4–$CoFe_2O_4$@MWCNT. The smallest Tafel slope of $CoFe_2O_4$@MWCNT electrocatalyst then pristine Co_3O_4–$CoFe_2O_4$ exhibit that it has excellent reaction kinetics and electron transfer efficiency for hydrogen evolution reaction.

Mechanism analysis using Tafel slope data requires a discussion of the fundamental processes involved in H_2 production. It is important to elaborate on the different basic processes that contribute to H_2 evolution. Tafel slope values reveal the underlying mechanism occurring at the solid–liquid interface.[56] The three simple steps from eqn (8)–(10) that makeup hydrogen production in alkaline media are as follows:

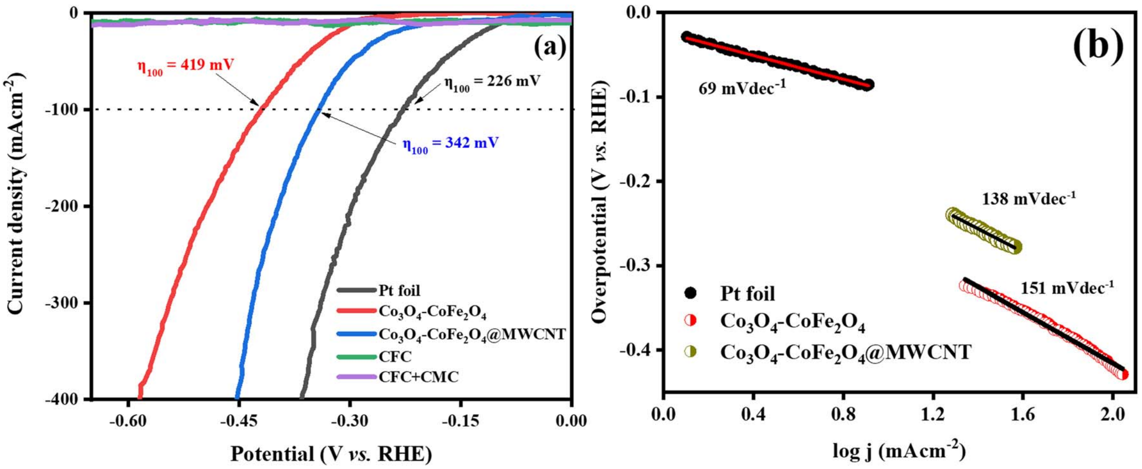

Fig. 7 (a) LSV polarization curve for HER activity of Pt, CFC, CFC with CMC binder, Co_3O_4–$CoFe_2O_4$, and Co_3O_4–$CoFe_2O_4$@MWCNT and their overpotential (η) values at $j = 100$ mA cm^{-2} and, (b) their corresponding Tafel slopes.

Table 3 OER and HER activity parameters of as-fabricated materials

		Tafel slope (mV dec^{-1})		Overpotential (mV) η_{100}		Onset potential (V)	
S. no.	Catalysts	OER	HER	OER	HER	OER	HER
1	Co_3O_4–$CoFe_2O_4$	220	151	333	419	1.50	0.376
2	Co_3O_4–$CoFe_2O_4$@MWCNT	166	138	290	342	1.49	0.331

$$* + \text{water mol.} + e^- \rightarrow \text{hydrogen radical} + OH^- \quad (8)$$

$$\text{Hydrogen radical} + \text{water mol.} + e^- \rightarrow \text{hydrogen gas}\uparrow + OH^- \quad (9)$$

$$2H^* \rightarrow \text{hydrogen gas}\uparrow + 2(*) \quad (10)$$

whereas, H_2 adsorbed to metal sites is denoted by H*, where * stands for active sites. The adsorption of water molecules on the surface of materials to form hydrogen radicals is the first and most widely accepted step in the HER mechanism and is widely considered to be the rate-determining step. Following this, the activated H* will either adsorb another unit of water molecule during the Heyrovsky reaction. A total of two water molecules are used in the HER process to generate one hydrogen molecule [$2H_2O + M^* + 2e \rightarrow H_2 + 2OH$].[57] According to the slope value of the Tafel plot for Co_3O_4–$CoFe_2O_4$@MWCNT, the Heyrovsky reaction is the rate-determining step during the HER electrocatalysis process.[58] In this study, Co_3O_4–$CoFe_2O_4$@MWCNT demonstrated impressive catalytic activity toward HER. Insufficient adsorption of H^+ ions onto the surface of Co_3O_4–$CoFe_2O_4$ may contribute to the material's poor performance toward HER. In summary, the synthesis of MWCNTs incorporated dual-phased Co_3O_4–$CoFe_2O_4$ is a promising approach to enhance the electrocatalytic HER activity in an aqueous alkaline solution. OER and HER activity parameters of as-fabricated materials are presented in Table 3.

Mott–Schottky examination of the as-prepared materials was carried out as depicted in Fig. 8. Analysis was used to know more about the electronic properties of Co_3O_4–$CoFe_2O_4$ and Co_3O_4–$CoFe_2O_4$@MWCNT. And also, this analysis was very useful for the calculation of their flat band potentials values and carrier densities of as-fabricated materials.[59] The potential for the flat band can be determined by plotting the linear portion of the curve against the *X*-axis of the Mott–Schottky plot.[60]

$$\frac{1}{C^2} = -\frac{2}{\varepsilon\varepsilon_0 e N_D}\left(E - E_{fb} - \frac{k_B T}{q}\right) \quad (11)$$

Flat-band potential (E_{fb}), specific capacitance (C), electron charge (e), dielectric constant (ε), vacuum permittivity (ε_0), carrier density (N_D), applied potential (E), Boltzmann constant (k), and absolute temperature (T) are all variables in this equation. The flat band potential of a material is the potential at which there is no net charge transfer between the material and the surrounding electrolyte.[61] The obtained E_{fb} for Co_3O_4–$CoFe_2O_4$ and Co_3O_4–$CoFe_2O_4$@MWCNT was 0.84 V and 0.73 V, respectively. A decrease in the flat band potential of Co_3O_4–$CoFe_2O_4$@MWCNT can result in a change in the electrochemical potential of the material, which can drive the creation of oxygen vacancies (OVs) through an electrochemical reaction. These vacancies can act as active sites for water oxidation, thereby improving the bifunctional electrocatalytic performance of the material. Obtained results show that the as-synthesized electrocatalyst is an efficient material as it has a higher value of charge carrier density which suggested the formation of oxygen vacancies in the material. The calculated carrier densities of both samples are given in Table 4. The lower flat band potential and improvement in charge carrier density

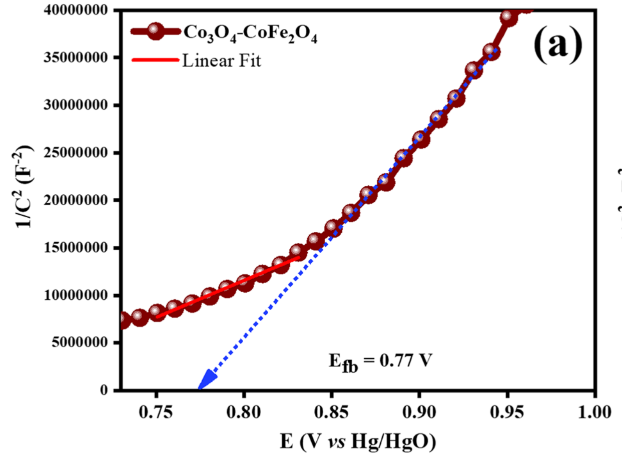

Fig. 8 Mott–Schottky profiles of as-synthesized catalysts for determination of flat band potential values: (a) Co_3O_4–$CoFe_2O_4$, and (b) Co_3O_4–$CoFe_2O_4$@MWCNT.

Table 4 EIS and Mott–Schottky results of different electrocatalysts synthesized in current study

S. no.	Catalysts	R_{ct} (Ω)	Exchange current density (mA cm^{-2})	Flat band potential (V)	Carrier density (×10^{23} cm^{-3})
1	Co_3O_4–$CoFe_2O_4$	2.87	2.24	0.77	8.63
2	Co_3O_4–$CoFe_2O_4$@MWCNT	1.72	3.73	0.73	74.0

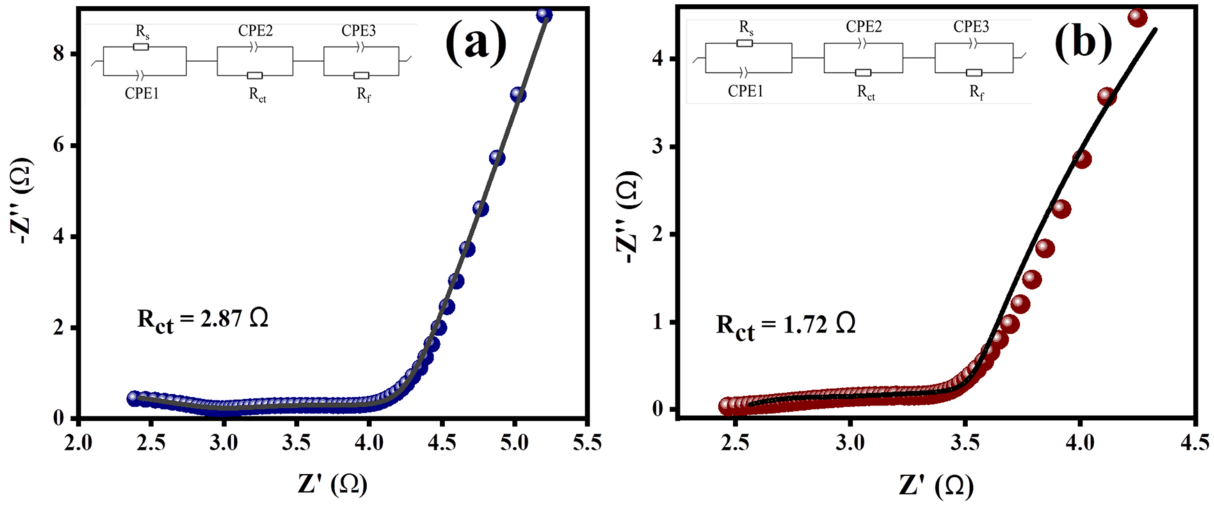

Fig. 9 EIS plots of as-prepared catalysts with fitted Randles circuit: (a) Co_3O_4–$CoFe_2O_4$, and (b) Co_3O_4–$CoFe_2O_4$@MWCNT electrocatalysts.

in Co_3O_4–$CoFe_2O_4$@MWCNT material was attributed to the formation of OVs in the as-prepared material which then act as electron donors.[62,63]

EIS analysis was performed on both samples to assume the kinetics of charge transfer between electrodes and electrolytes.[64] Nyquist plots obtained from EIS measurements are displayed in Fig. 9. The Nyquist plot was taken over the frequency span of 10 000 to 0.01 Hz. The experimental EIS data was depicted using a modified Randles circuit. The finalized circuit diagram appears in the inlays of Fig. 10.

This circuit displays the solution resistance R_s, the R_{ct} refers to charge transfer resistance, and the film resistance R_f of the layer formed on the CFC. The performance of the HER and OER between the liquid phase and electrode is greatly influenced by the charge-transfer resistance (R_{ct}), which is present in the high-end frequency region of the first semicircle. For Co_3O_4–$CoFe_2O_4$ and $CoFe_2O_4$@MWCNT, the calculated R_{ct} values were 2.87 Ω and 1.72 Ω, respectively. The faster electron-transfer process at the surfaces of the Co_3O_4–$CoFe_2O_4$@MWCNT electrocatalysts was inferred from their lower R_{ct}.[65] The charge-trapping effect of

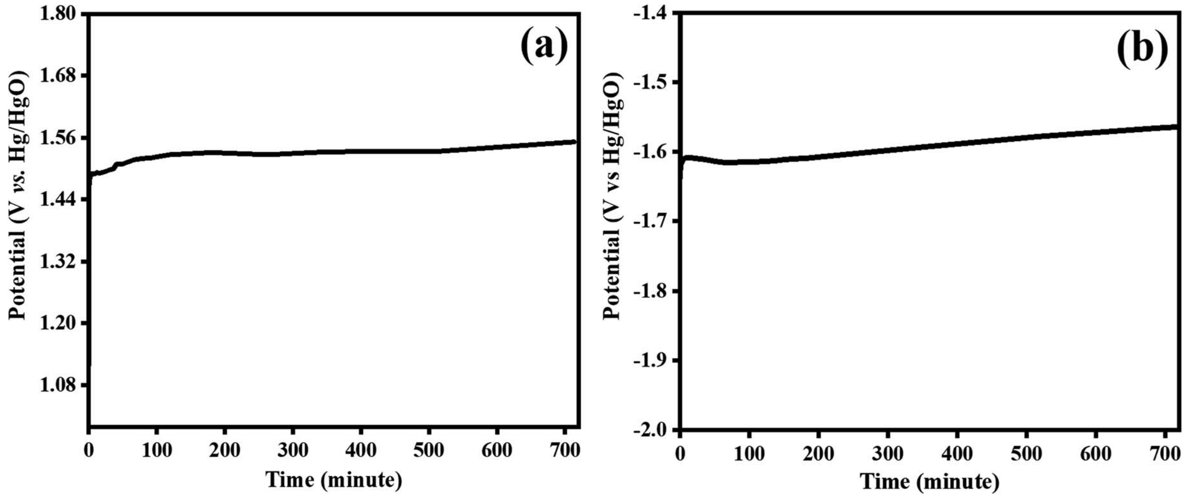

Fig. 10 Stability test for bifunctional Co_3O_4–$CoFe_2O_4$@MWCNT electrocatalyst at 100 mA cm^{-2} for an extended period 720 minutes; (a) OER and, (b) HER electrocatalysis.

Table 5 Comparative studies of the bifunctional Co_3O_4–$CoFe_2O_4$@MWCNT electrocatalyst with previously reported literature

			Overpotential (mV)		Tafel slope (mV dec^{-1})		
Electrocatalysts	Electrolyte	Method of synthesis	OER	HER	OER	HER	Ref.
Co_3O_4–$CoFe_2O_4$@MWCNT	1 M KOH	Ultrasonication	$\eta_{100} = 290$	$\eta_{100} = 342$	166	138	This work
NF/Co_3O_4–$CoFe_2O_4$	0.1 M K_3BO_3	Solvothermal	$\eta_{10} = 215$	—	90	—	67
$CoFe_2O_4$/SWCNTs	1 M KOH	Hydrothermal	$\eta_{10} = 310$	$\eta_{10} = 263$	85	46	68
Co_3O_4/SWCNTs	1 mol L^{-1} KOH	Self-assembly	$\eta_{10} = 430$	—	104	—	69
Co_3O_4@CoWP	1.0 M KOH	Hydrothermal	$\eta_{10} = 269$	$\eta_{10} = 118$ mV	69	58	70
Co_3O_4-ZIF8	1 M KOH	Hydrothermal	$\eta_1 = 270$	—	82	—	71
$CoFe_2O_4$	0.5 M H_2SO_4	Hydrothermal	—	$\eta_{10} = 45$	—	35	72
Cu_2O–Co_3O_4/CN	1 M KOH	Hydrothermal	$\eta_{10} = 396$	—	281	—	73
SC-CoO_x NPs	0.1 M KOH	Spray-coating	300	350	54	133	74

MWCNTs, the decrease in flat-band potential, and the increase in charge-carrier density governed this decrease in charge-transfer resistance. The charge was able to flow more freely across the Co_3O_4–$CoFe_2O_4$@MWCNT/electrolyte interfaces as a result of this effect. The exchange current density (J^0) was further analyzed to reveal the vital behavior of the entire water-splitting reaction and the consequences of charge-transfer resistance.[66] The J^0 was determined by using this formula: $J^0 = (R \times T)/(A \times n \times F \times q)$, where R stands for universal gas constant, T is abbreviated as the absolute temperature, the geometric area of the electrode is represented by A, F refers to Faraday's constant, q represents charge-transfer resistance and n denotes number of electrons in the charge being transferred. The Co_3O_4–$CoFe_2O_4$ binary and Co_3O_4–$CoFe_2O_4$@MWCNT ternary composite produced exchange current densities of 2.24 mA cm^{-2} and 3.73 mA cm^{-2}, respectively. Co_3O_4–$CoFe_2O_4$@MWCNT electrocatalyst's high intrinsic activity was demonstrated by the greater value of exchange current density with faster charge transfer across the electrode interphase.

3.4.2. Stability tests. One more factor to consider when assessing the practical application of prepared materials as electrocatalyst is their long-term stability. Applying a steady current density of 100 mA cm^{-2} for 720 minutes was used to observe the long-term stability of the Co_3O_4–$CoFe_2O_4$@MWCNT electrocatalyst during OER and HER electrocatalysis. The tested electrocatalyst potential was not significantly impacted by the extended chronopotentiometry testing (Fig. 10), demonstrating the composite steadiness and outstanding stability for water splitting. The extended interconnected network of Co_3O_4–$CoFe_2O_4$ and MWCNT contributes to the material's outstanding long-term stability. Superior OER and HER bifunctional catalytic activity of the Co_3O_4–$CoFe_2O_4$/MWCNT catalyst may result from the MWCNT's high number of redox sites and enhanced electronic conduction. The comparison of current studies with previously reported literature is given in Table 5.

4. Conclusion

In summary, the pristine Co_3O_4–$CoFe_2O_4$ and Co_3O_4–$CoFe_2O_4$@MWCNT electrocatalysts with nano-rocks-like amorphous structures were prepared by using sonochemical activation route for bifunctional OER/HER performances, employing three electrode setups. Co_3O_4–$CoFe_2O_4$@MWCNT/CFC electrodes exhibit outstanding OER and HER dual-functional electrocatalytic efficiency and stability which may be attributed to the presence of MWCNT which facilitates higher conductivity, superior charge transfer kinetics, and provides greater number of active sites for the water splitting reactions. The Co_3O_4–$CoFe_2O_4$@MWCNT catalyst shows superior electrocatalytic activity towards OER and HER with minimum overpotential required for attaining a high current density of 100 mA cm^{-2} as compared to its counterpart samples. The as-prepared Co_3O_4–$CoFe_2O_4$@MWCNT electrocatalyst has an improved electrochemical active surface area of 6.5625 cm^2, minimum charge transfer resistance of 1.72 Ω, and a higher exchange current density of 3.73 mA cm^{-2} due to which it shows exceptional properties in water splitting with a higher rate kinetics. In this work, the catalyst with high stability and electrocatalytic activity has been designed for enhanced water splitting in an alkaline medium which is prepared through easy, large-scale, and cheap methods.

Conflicts of interest

All authors of this manuscript declare no conflict of interest being published in this journal.

Acknowledgements

The researchers would like to acknowledge Deanship of Scientific Research, Taif University for funding this work. Authors are also thankful to the Institute of Chemistry, BJ Campus, The Islamia University of Bahawalpur-Pakistan and HEC-Islamabad (Pakistan).

References

1 H.-M. Yang and Z.-Y. Yuan, in *Transition Metal-Based Electrocatalysts: Applications in Green Hydrogen Production and Storage*, American Chemical Society, 2023, vol. 1435, ch. 1, pp. 1–20.

2 B. Mohanty, P. Bhanja and B. K. Jena, *Mater. Today Energy*, 2022, **23**, 100902.

3 M. Kaleemullah, S. Yousaf, I. A. Alsafari, H. H. Somaily, J. Rahman, M. Shahid, M. Ashraf and M. F. Warsi, *Int. J. Environ. Anal. Chem.*, 2022, 1–14, DOI: **10.1080/03067319.2022.2141117**.

4 A. Mustafa, I. A. Alsafari, H. H. Somaily, S. Yousaf, M. I. Din, J. Rahman, M. Shahid, M. Ashraf and M. F. Warsi, *Phys. B*, 2023, **648**, 414404.

5 S. Rafiq, M. Aadil, M. F. Warsi, S. Yousaf, M. T. Alotaibi, S. M. El-Bahy and M. Shahid, *Ceram. Int.*, 2022, **48**, 14596–14605.

6 S. Rafiq, A. K. Alanazi, S. Bashir, A. Y. Elnaggar, G. A. M. Mersal, M. M. Ibrahim, S. Yousaf and K. Chaudhary, *Phys. B*, 2022, **638**, 413931.

7 S. Yousaf, M. Aadil, S. Zulfiqar, M. F. Warsi, P. O. Agboola, M. F. Aly Aboud and I. Shakir, *J. Mater. Res. Technol.*, 2020, **9**, 14158–14167.

8 S. Yousaf, S. Zulfiqar, M. Shahid, A. Jamil, I. Shakir, P. O. Agboola and M. F. Warsi, *Ceram. Int.*, 2020, **46**, 14304–14310.

9 S. Wang, A. Lu and C. J. Zhong, *Nano Convergence*, 2021, **8**(1), 1–4.

10 S. Wang, A. Lu and C.-J. Zhong, *Nano Convergence*, 2021, **8**, 4.

11 K. M. Katubi, A.-Z. Warsi, F. Aziz, Z. A. K. Khattak, M. F. Warsi, M. S. Al-Buriahi, Z. A. Alrowaili and S. Yousaf, *Curr. Appl. Phys.*, 2023, **51**, 80–90.

12 B. M. Stühmeier, M. R. Pietsch, J. N. Schwämmlein and H. A. Gasteiger, *J. Electrochem. Soc.*, 2021, **168**, 064516.

13 C. Li and J.-B. Baek, *ACS Omega*, 2020, **5**, 31–40.

14 M. Tahir, L. Pan, F. Idrees, X. Zhang, L. Wang, J.-J. Zou and Z. L. Wang, *Nano Energy*, 2017, **37**, 136–157.

15 J. Liu, J. Ma, Z. Zhang, Y. Qin, Y.-J. Wang, Y. Wang, R. Tan, X. Duan, T. Z. Tian and C. H. Zhang, *J. Phys.: Mater.*, 2021, **4**, 022004.

16 S. Sanati, A. Morsali and H. García, *Energy Environ. Sci.*, 2022, **15**, 3119–3151.

17 Y. Liu, Y. Guo, Y. Liu, Z. Wei, K. Wang and Z. Shi, *Energy Fuels*, 2023, **37**, 2608–2630.

18 Y. Wang, C. Yang, Z. Li, Z. Liang and G. Cao, *Small*, 2020, **16**(25), 2001973.

19 J. Li, J. Li, X. Zhou, Z. Xia, W. Gao, Y. Ma and Y. Qu, *ACS Appl. Mater. Interfaces*, 2016, **8**, 10826–10834.

20 Y. Lv, M. Chen, N. Suo, X. He and L. Cui, *J. Electroanal. Chem.*, 2022, **927**, 116979.

21 F. Shahbazi Farahani, M. S. Rahmanifar, A. Noori, M. F. El-Kady, N. Hassani, M. Neek-Amal, R. B. Kaner and M. F. Mousavi, *J. Am. Chem. Soc.*, 2022, **144**, 3411–3428.

22 X. Chen, J. Liu, T. Yuan, Z. Zhang, C. Song, S. Yang, X. Gao, N. Wang and L. Cui, *Energy Mater.*, 2022, **2**, 200028.

23 D. H. Taffa, D. Balkenhohl, M. Amiri and M. Wark, *Small Struct.*, 2023, **4**(6), 2200263.

24 J. Wang, X. Yue, Y. Yang, S. Sirisomboonchai, P. Wang, X. Ma, A. Abudula and G. Guan, *J. Alloys Compd.*, 2020, **819**, 153346.

25 K. B. Ibrahim, M.-C. Tsai, S. A. Chala, M. K. Berihun, A. W. Kahsay, T. A. Berhe, W.-N. Su and B.-J. Hwang, *J. Chin. Chem. Soc.*, 2019, **66**, 829–865.

26 J. Kubisztal and M. Kubisztal, *Catalysts*, 2022, **12**, 21.

27 X.-M. Liu, X. Cui, K. Dastafkan, H.-F. Wang, C. Tang, C. Zhao, A. Chen, C. He, M. Han and Q. Zhang, *J. Energy Chem.*, 2021, **53**, 290–302.

28 S. Zhu, J. Lei, Y. Qin, L. Zhang and L. Lu, *RSC Adv.*, 2019, **9**, 13269–13274.

29 G. Ou, F. Wu, K. Huang, N. Hussain, D. Zu, H. Wei, B. Ge, H. Yao, L. Liu, H. Li, Y. Shi and H. Wu, *ACS Appl. Mater. Interfaces*, 2019, **11**, 3978–3983.

30 A. Wang, X. Chen, L. Cheng, X. Shen, W. Zhu, L. Li and J. Pang, *J. Mater. Chem. A*, 2020, **8**, 17621–17633.

31 Y. Meng, X. Huang, H. Lin, P. Zhang, Q. Gao and W. Li, *Front. Chem.*, 2019, **7**, 759.

32 P. Ravi, V. Navakoteswara Rao, M. V. Shankar and M. Sathish, *Mater. Today Energy*, 2021, **21**, 100779.

33 R. Koutavarapu, S. G. Peera, T. G. Lee, C. R. Myla, D.-Y. Lee, J. Shim and S. K. Balasingam, *Processes*, 2021, **9**, 1959.

34 S. Chamani, M. Khatamian, N. S. Peighambardoust and U. Aydemir, *ACS Omega*, 2021, **6**, 33024–33032.

35 E. Sadeghi, N. S. Peighambardoust, S. Chamani and U. Aydemir, *ACS Mater. Au*, 2023, **3**, 143–163.

36 H. H. Al-Rasheed, M. Al Alshaikh, J. M. Khaled, N. S. Alharbi and A. El-Faham, *J. Chem.*, 2016, **2016**, 3464758.

37 S. V. Sancheti and P. R. Gogate, *Ultrason. Sonochem.*, 2017, **36**, 527–543.

38 N. F. Andrade Neto, A. B. Lima, R. R. Y. O. V. Wilson, T. C. N. Nicacio, M. R. D. Bomio and F. V. Motta, *Mater. Sci. Semicond. Process.*, 2022, **139**, 106311.

39 K. Kawashima, R. A. Márquez, Y. J. Son, C. Guo, R. R. Vaidyula, L. A. Smith, C. E. Chukwuneke and C. B. Mullins, *ACS Catal.*, 2023, **13**, 1893–1898.

40 A. Moysiadou, S. Lee, C.-S. Hsu, H. M. Chen and X. Hu, *J. Am. Chem. Soc.*, 2020, **142**, 11901–11914.

41 T. A. Centeno and F. Stoeckli, *J. Power Sources*, 2006, **154**, 314–320.

42 L. Kafi-Ahmadi, S. Khademinia, M. Najafzadeh Nansa, A. A. Alemi, M. Mahdavi and A. Poursattar Marjani, *J. Chil. Chem. Soc.*, 2020, **65**, 4845–4848.

43 H. Ebrahimzade, G. R. Khayati and M. Schaffie, *Adv. Powder Technol.*, 2017, **28**, 2779–2786.

44 J. Li, y. Senbin, T. Li, X. Li, X. Yang and S. Ding, *Procedia Eng.*, 2015, **102**, 492–498.

45 X. Sun, C. Zheng, F. Zhang, Y. Yang, G. Wu, A. Yu and N. Guan, *J. Phys. Chem. C*, 2009, **113**, 16002–16008.

46 M. Aghazadeh and F. Aghazadeh, *Int. J. Bio-Inorg. Hybrid Nanomater.*, 2018, **7**, 97–108.

47 R. A. Bohara, N. D. Thorat, H. M. Yadav and S. H. Pawar, *New J. Chem.*, 2014, **38**, 2979–2986.

48 R. Bhargava, S. Khan, N. Ahmad and M. M. N. Ansari, *AIP Conf. Proc.*, 2018, 1953.

49 D. Karthickraja, S. Karthi, G. A. Kumar, D. K. Sardar, G. C. Dannangoda, K. S. Martirosyan and E. K. Girija, *New J. Chem.*, 2019, **43**, 13584–13593.

50 Y. Mao, B. Zhou and S. Peng, *J. Mater. Sci.: Mater. Electron.*, 2020, **31**, 9457–9467.

51 S. Yousaf, S. Zulfiqar, H. H. Somaily, M. F. Warsi, A. Rasheed, M. Shahid and I. Ahmad, *RSC Adv.*, 2022, **12**, 23454–23465.

52 N.-U.-A. Babar, F. Hussain, M. N. Ashiq and K. S. Joya, *ACS Appl. Energy Mater.*, 2021, **4**, 8953–8968.

53 A. Kapałka, G. Fóti and C. Comninellis, *Electrochem. Commun.*, 2008, **10**, 607–610.

54 N. Alwadai, S. Manzoor, S. R. Ejaz, R. Y. Khosa, S. Aman, M. Al-Buriahi, S. Alomairy, Z. Alrowaili, H. Somaily and M. Hayat, *J. Mater. Sci.: Mater. Electron.*, 2022, **33**, 13244–13254.

55 P. V. Shinde, R. Samal and C. S. Rout, *Trans. Tianjin Univ.*, 2022, **28**, 80–88.

56 Y. Jiang, J. Huang, B. Mao, T. An, J. Wang and M. Cao, *Appl. Catal., B*, 2021, **293**, 120220.

57 K. Srinivas, Y. Chen, Z. Su, B. Yu, M. Karpuraranjith, F. Ma, X. Wang, W. Zhang and D. Yang, *Electrochim. Acta*, 2022, **404**, 139745.

58 H. Zhong, C. A. Campos-Roldán, Y. Zhao, S. Zhang, Y. Feng and N. Alonso-Vante, *Catalysts*, 2018, **8**, 559.

59 N. Lele, M. F. Bambo, E. M. Mmutlane and L. N. Dlamini, *Emergent Mater.*, 2023, **6**, 605–626.

60 P. F. Ndione, E. L. Ratcliff, S. R. Dey, E. L. Warren, H. Peng, A. M. Holder, S. Lany, B. P. Gorman, M. M. Al-Jassim, T. G. Deutsch, A. Zakutayev and D. S. Ginley, *ACS Omega*, 2019, **4**, 7436–7447.

61 S. Al-Hilli and M. Willander, *Sensors*, 2009, **9**, 7445–7480.

62 S. Wang, T. He, P. Chen, A. Du, K. Ostrikov, W. Huang and L. Wang, *Adv. Mater.*, 2020, **32**, 2001385.

63 X. Wu, F. E. Oropeza, D. den Boer, P. Kleinschmidt, T. Hannappel, D. G. H. Hetterscheid, E. J. M. Hensen and J. P. Hofmann, *ChemPhotoChem*, 2023, **7**, e202200192.

64 N. O. Laschuk, E. B. Easton and O. V. Zenkina, *RSC Adv.*, 2021, **11**, 27925–27936.

65 W. Zhang, B. Jia, X. Liu and T. Ma, *SmartMat*, 2022, **3**, 5–34.

66 Z. Zhang, Y. Wang, X. Leng, V. H. Crespi, F. Kang and R. Lv, *ACS Appl. Energy Mater.*, 2018, **1**, 1268–1275.

67 M. Nozari-Asbemarz, M. Amiri, A. Khodayari, A. Bezaatpour, S. Nouhi, P. Hosseini, M. Wark, R. Boukherroub and S. Szunerits, *ACS Appl. Energy Mater.*, 2021, **4**, 2951–2959.

68 Y. Ding, J. Zhao, W. Zhang, J. Zhang, X. Chen, F. Yang and X. Zhang, *ACS Appl. Energy Mater.*, 2018, **2**, 1026–1032.

69 J. Wu, Y. Xue, X. Yan, W. Yan, Q. Cheng and Y. Xie, *Nano Res.*, 2012, **5**, 521–530.

70 L. Zhang, T. Zhang, K. Dai, L. Zhao, Q. Wei, B. Zhang and X. Xiang, *RSC Adv.*, 2020, **10**, 29326–29335.

71 G. Wei, Z. Zhou, X. Zhao and C. An, *ACS Appl. Mater. Interfaces*, 2019, **10**(28), 23721.

72 J. Yin, L. Shen, Y. Li, M. Lu, K. Sun and P. Xi, *J. Mater. Res.*, 2018, **33**, 590–600.

73 Z. A. Shaikh, N. Moiseev, A. Mikhaylov and S. Yüksel, *Appl. Sci.*, 2021, **11**, 9974.

74 N.-U.-A. Babar, M. Asghar, F. Hussain and K. Joya, *Mater. Today Energy*, 2020, **17**, 100434.